1
2
3
4
5
6
7
8
9
10
11
12
13
14
15
16
17
18
19
20
21
22
23
24
25
26
27
28
29
30
31
32
33
34
35
36
37
38
39
40
41
42
43
44
45
46
47

Optimization of Intensities and Orientations of Magnets Controlling Melt Flow During Solidification

George S. Dulikravich,[1,*] Marcelo J. Colaço,[2] Brian H. Dennis,[3] Thomas Martin,[4] Igor N. Egorov-Yegorov,[5] and Seungsoo Lee[6]

AQ1

[1]Florida International University, Mechanical and Materials Eng. Dept., MAIDROC Lab., Miami, FL, USA
[2]Military Institute of Engineering (IME), Mechanical and Materials Eng. Dept., Rio de Janeiro, Brazil
[3]University of Texas at Arlington, Mechanical and Aerospace Eng. Dept., Arlington, TX, USA
[4]Pratt and Whitney Engine Company, Turbine Discipline Engineering and Optimization Group, East Hartford, CT, USA
[5]Sigma Technology, Moscow, Russia
[6]Inha University, Aerospace Eng. Dept., Incheon, Korea

ABSTRACT

When growing large single crystals from a melt, it is desirable to minimize thermally induced convection effects so that solidification is achieved predominantly by thermal conduction. It is expected that under such conditions any impurities that originate from the walls of the crucible will be less likely to migrate into the mushy region and consequently deposit in the crystal. It is also desirable to achieve a distribution of the dopant in the crystal that is as uniform as possible. A finite volume method and a least-squares spectral finite element method were used to develop accurate computer codes for prediction of solidification from a melt

*Correspondence: Prof. George S. Dulikravich, Florida International University, Mechanical and Materials Eng. Dept., MAIDROC Lab., EC 3474, Miami, FL 33027, USA; E-mail: dulikrav@fiu.edu.

1

+ [12.8.2004–7:54pm] [1–24] [Page No. 2]
K./Journals/Inpro/MDI/LMMP/LMMP19(4)/200031887.3d Materials and Manufacturing Processes (LMMP)

200031887_LMMP19_04_R1_081204

2   S. Dulikravich et al.

under the influence of externally applied magnetic fields. A hybrid constrained optimization algorithm and a semi-stochastic self-adapting response surface optimizer were then used with these solidification analysis codes to determine the distributions of the magnets that will minimize the convective flow throughout the melt or in desired regions of the melt only.

AQ2

INTRODUCTION

The objective of this article is to demonstrate the feasibility of determining unknown boundary values of an applied magnetic field that will create user-specified features of the melt flow-field and the melt/solid interface. This article presents a proof-of-concept effort and it does not present the most advanced MHD analysis involving solidification. In this study, all physical properties (density, heat conductivity, heat capacity, electric conductivity, etc.) were treated as constants instead of as functions of temperature. The effects of magnetization were not included. This study does not involve optimization of thermal boundary conditions in MHD solidification.[1]

The latent heat released in the mushy region of a solidifying melt, where $T_{\text{liquidus}} > T > T_{\text{solidus}}$, is assumed to be proportional to the local volumetric liquid/(liquid + solid) ratio.[2,3]

$$f = \frac{V_\ell}{V_\ell + V_s} = \left(\frac{T - T_{\text{solidus}}}{T_{\text{liquidus}} - T_{\text{solidus}}} \right)^n = \tilde{\theta}^n \tag{1}$$

Here, the exponent n is typically $0.2 < n < 5$, while $f = 1$ for $T \geq T_{\text{liquidus}}$ and $f = 0$ for $T \leq T_{\text{solidus}}$. In all test cases, the non-dimensional temperature is given as

$$\theta = \frac{T - T_{\text{solidus}}}{T_h - T_c} \tag{2}$$

Thus, $\theta = 0.0$ corresponds to interface between the solid phase and the mushy region. For relatively small changes of density with temperature, it is justifiable to assume linear variation of density as a function of the temperature.[4] In the liquid, the density is

$$\rho_\ell = \rho_r \left[1 + \left(\frac{\partial(\rho_\ell / \rho_r)}{\partial \theta} \right)_r (\theta - \theta_r) \right] = \rho_r [1 - \alpha_\ell (\theta - \theta_r)] \tag{3}$$

with a similar expression for the solid phase. Therefore, the liquid–solid mixture density and modified heat capacity can be defined as

$$\rho_{\text{mix}} = f \rho_\ell + (1 - f) \rho_s \tag{4}$$

$$c_{\text{mix}} = f \rho_\ell \frac{\partial(c_\ell \theta_\ell)}{\partial \theta} + (1 - f) \rho_s \frac{\partial(c_s^{eq} \theta_s)}{\partial \theta} \tag{5}$$

where an enthalpy method[3] was used to formulate the equivalent specific heat coefficient in the solid phase.

$$c_s^{eq} = c_s - \frac{1}{S_{TE}} \frac{\partial L}{\partial \theta} \tag{6}$$

Here, the specific heat coefficient accounts for the latent heat release in the mushy region. The non-dimensional numbers used in magneto-hydrodynamics (MHD) modeling are as follows:

Reynolds hydrodynamic   Prandtl hydrodynamic   Eckert number

$$R_e = \frac{\rho_r v_r \ell_r}{\mu_{vr}} \qquad P_R = \frac{\mu_{vr} c_r}{\kappa_r} \qquad E_c = \frac{v_r^2}{c_r \Delta T_r} \tag{7a--c}$$

Grash of number   Prandtl magnetic   Hartmann number

$$G_R = \frac{\rho_r^2 \alpha_r g_r \Delta T_r \ell_r^3}{\mu_{vr}^2} \qquad P_m = \frac{\mu_{vr} \sigma_r \mu_r}{\rho_r} \qquad H_T = \ell_r \mu_r H_r \left(\frac{\sigma_r}{\mu_{vr}}\right)^{1/2} \tag{7d--f}$$

Stefan number   Froude number   Rayleigh number

$$S_{TE} = \frac{c_r \Delta T_r}{L_r} \qquad F_R = \frac{v_r^2}{g_r \ell_r} \qquad R_a = \frac{\rho_r^2 \alpha_r c_r g_r \Delta T_r \ell_r^3}{\kappa_r \mu_{vr}} \tag{7g--i}$$

Using these parameters, the non-dimensional formulation of the Navier-Stokes subsystem of the MHD equations for phase-changing mixtures of two liquids has been formulated.[5--7] In this formulation, the solid phase is treated as the second liquid with extremely high viscosity. Assuming that both phases have the same local velocity, the non-dimensional form of mass conservation is obvious.

$$\nabla \cdot \underline{v} = 0 \tag{8}$$

Each phase could have been modeled with its own velocity, which would yield a more complicated expression for multi-component mass conservation.[8] The non-dimensional version of linear momentum conservation for two-phase MHD flows with thermal buoyancy, and magnetic force is

$$\rho_{\text{mix}} \frac{\partial \underline{v}}{\partial t} + f \rho_\ell \nabla \cdot (\underline{vv} + \hat{p}_\ell \underline{I}) + (1 - f) \rho_s \nabla \cdot (\underline{vv} + \hat{p}_s \underline{I})$$

$$= f \left\{ \nabla \cdot \left[\frac{\mu_{v\ell}}{R_e} (\nabla \underline{v} + (\nabla \underline{v})^*) \right] + \frac{G_R}{R_e^2} \rho_\ell \alpha_\ell \theta \, \underline{g} + \frac{H_T^2}{P_m R_e^2} \mu_\ell (\nabla \times \underline{H}) \times \underline{H} \right\}$$

$$+ (1 - f) \left\{ \nabla \cdot \left[\frac{\mu_{vs}}{R_e} (\nabla \underline{v} + (\nabla \underline{v})^*) \right] + \frac{G_R}{R_e^2} \rho_s \alpha_s \theta \, \underline{g} + \frac{H_T^2}{P_m R_e^2} \mu_s (\nabla \times \underline{H}) \times \underline{H} \right\} \tag{9}$$

where the non-dimensional hydrodynamic, hydrostatic, and magnetic pressures were combined to give

$$\hat{p}_\ell = \frac{p}{\rho_\ell} + \frac{\varphi}{F_R^2} + \frac{H_T^2}{P_m R_e^2} \mu_\ell \underline{H} \cdot \underline{H} \quad \text{and} \quad \hat{p}_s = \frac{p}{\rho_s} + \frac{\varphi}{F_R^2} + \frac{H_T^2}{P_m R_e^2} \mu_s \underline{H} \cdot \underline{H} \tag{10}$$

+   [12.8.2004–7:54pm]   [1–24]   [Page No. 4]
K./Journals/Inpro/MDI/LMMP/LMMP19(4)/200031887.3d   Materials and Manufacturing Processes (LMMP)

200031887_LMMP19_04_R1_081204

4   S. Dulikravich et al.

Here, φ is the non-dimensional gravity potential defined as $\underline{g} = -\nabla\varphi$. Then, the non-dimensional form of energy conservation for incompressible phase-changing MHD flows including Joule heating can be written as[6]

$$c_{\text{mix}}\frac{\partial\theta}{\partial t} + f\rho_\ell\nabla\cdot(c_\ell\theta\underline{v}) + (1-f)\rho_s\nabla\cdot(c_s^{eq}\theta\underline{v})$$

$$= f\left[\frac{1}{R_e P_R}\nabla\cdot(\kappa_\ell\nabla\theta) + \frac{1}{\sigma_\ell}\frac{H_T^2 E_c}{P_m^2 R_e^3}(\nabla\times\underline{H})\cdot(\nabla\times\underline{H})\right]$$

$$+ (1-f)\left[\frac{1}{R_e P_R}\nabla\cdot(\kappa_s\nabla\theta) + \frac{1}{\sigma_s}\frac{H_T^2 E_c}{P_m^2 R_e^3}(\nabla\times\underline{H})\cdot(\nabla\times\underline{H})\right] \tag{11}$$

The classical modeling of MHD assumes that there are no free electric charges in the fluid.[5,7] With these assumptions Maxwell's system for steady electro-magnetics of a moving media becomes

$$\nabla\cdot\underline{B} = 0 \tag{12}$$

$$\nabla\times\underline{H} = \underline{J} \tag{13}$$

$$\nabla\cdot\underline{J} = 0 \tag{14}$$

Ohm's law relates the induced electric current to the magnetic intensity vector in a moving media.

$$\underline{J} = \sigma\underline{v}\times\underline{B} \tag{15}$$

If electric conductivity and magnetic permeability are assumed to be constant within each phase, then the following non-dimensionalized magnetic field transport equation for the phase-changing MHD flow can be obtained from Eqs. (12) to (15). It needs to be solved intermittently[6] with Eqs. (8) through (11).

$$\frac{\partial\underline{H}}{\partial t} - \nabla\times(\underline{v}\times\underline{H}) = \frac{f/(\sigma_\ell\mu_\ell) + (1-f)/(\sigma_s\mu_s)}{P_m R_e}\nabla^2\underline{H} \tag{16}$$

The modified magnetic transport equations (16), the continuity equation (8), the modified linear momentum balance equations (9), and the modified energy balance equation (11) were integrated numerically using a finite volume method for structured clustered grids written in terms of non-orthogonal boundary-conforming coordinates.[9] Artificial density formulation was used to remove the singularity from the Navier-Stokes system, and the artificial time integration was performed using a four-stage Runge-Kutta algorithm.

EXAMPLES OF COMPUTED MHD FLOWS WITH SOLIDIFICATION

First, let us consider the problem of steady state solidification in two square-shaped containers without any magnetic field. Each container had the following

Optimization of Intensities and Orientations

Table 1. Physical properties of molten and solid silicon.[9]

$\rho_\ell = 2550 \, \text{kg/m}^3$	$\rho_s = 2330 \, \text{kg/m}^3$
$c_p\ell = 1059 \, \text{J/kg K}$	$c_{ps} = 1038 \, \text{J/kg K}$
$\kappa_\ell = 64 \, \text{W/m K}$	$\kappa_s = 22 \, \text{W/m K}$
$T_\ell = 1685 \, \text{K}$	$T_s = 1681 \, \text{K}$
$\sigma_\ell = 12.3 \times 10^5 \, 1/\Omega \, \text{m}$	$\sigma_s = 4.3 \times 10^4 \, 1/\Omega \, \text{m}$
$\mu_{v\ell} = 7.018 \times 10^{-4} \, \text{kg/m s}$	$\mu = 7.022 \times 10^{-4} \, \text{kg m/A}^2 \, \text{s}^2$
$L = 1.803 \times 10^6 \, \text{J/kg}$	$\alpha = 1.4 \times 10^{-4} \, 1/\text{K}$

Table 2. Parameters for two test cases.

Case 1 (small container)	Case 2 (large container)
$l_r = 0.01 \, \text{m}$	$l_r = 0.02 \, \text{m}$
$\text{Re} = 1000$	$\text{Re} = 1000$
$B_r = 0.1 \, \text{T}$	$B_r = 0.1 \, \text{T}$
$v_r = 2.7522 \times 10^{-2} \, \text{m/s}$	$v_r = 1.3761 \times 10^{-2} \, \text{m/s}$
$\text{Pr} = 1.1613 \times 10^{-2}$	$\text{Pr} = 1.1613 \times 10^{-2}$
$\text{Gr} = 1.8132 \times 10^5$	$\text{Gr} = 1.4506 \times 10^6$
$\text{Ra} = 2.1056 \times 10^3$	$\text{Ra} = 1.6845 \times 10^4$
$\text{Fr} = 8.7870 \times 10^{-2}$	$\text{Fr} = 3.1067 \times 10^{-2}$
$\text{Ec} = 7.1524 \times 10^{-8}$	$\text{Ec} = 1.7881 \times 10^{-8}$
$\text{Ht} = 4.1864 \times 10^1$	$\text{Ht} = 8.3729 \times 10^1$

thermal boundary conditions: left wall at T_c, right wall at T_h, and top and bottom walls thermally insulated. Gravity was assumed to act vertically downwards. Physical properties of molten and solid silicon (Table 1) were used in these two example **T1** test cases.

The physical properties of the liquid phase from Table 1 were adopted as the reference properties. For $\Delta T_r = T_h - T_c = 10 \, \text{K}$, and $\text{Re} = 1000$, the resulting non-dimensional parameters are given in Table 2 for two different sizes of solidification **T2** containers, it should be noted out that these test cases used the physical properties for silicon with one exception. The magnetic Prandtl number that was used was three orders of magnitude larger than its physical value. This was done because the realistic extremely small values of P_m caused the explicit numerical integration algorithm used in the MHD analysis to diverge.

Figures 1 and 2 present the results for both test cases without magnetic field **F1 F2** applied ($\text{Ht} = 0.0$) using two different grid sizes.
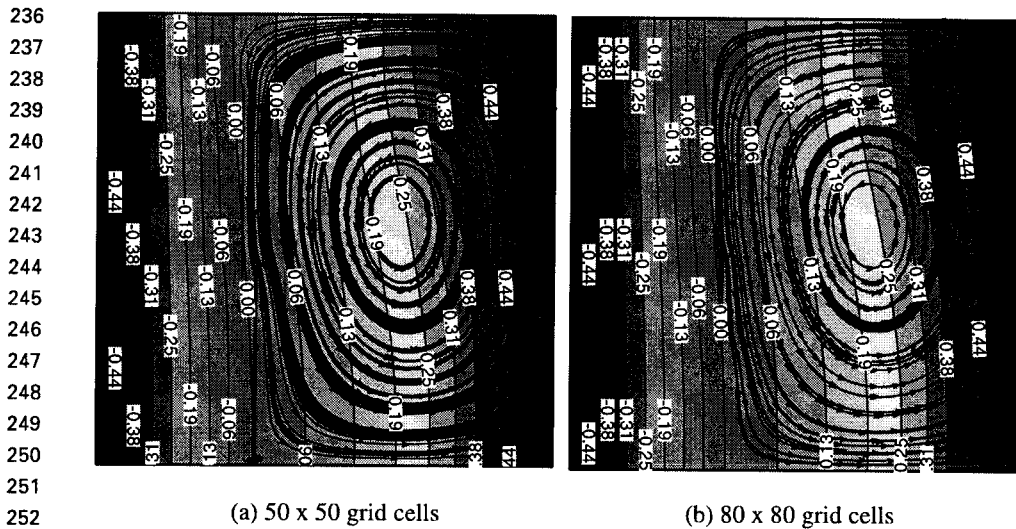
In both test cases, the results for the coarser grid (50×50 grid cells) are very similar to the results with a refined grid (80×80 grid cells). The coarser grid was used for the MHD solidification simulations during the optimization process. Figure 3 shows the convergence history for containers of both sizes when using a grid **F3** size of 50×50 grid cells.
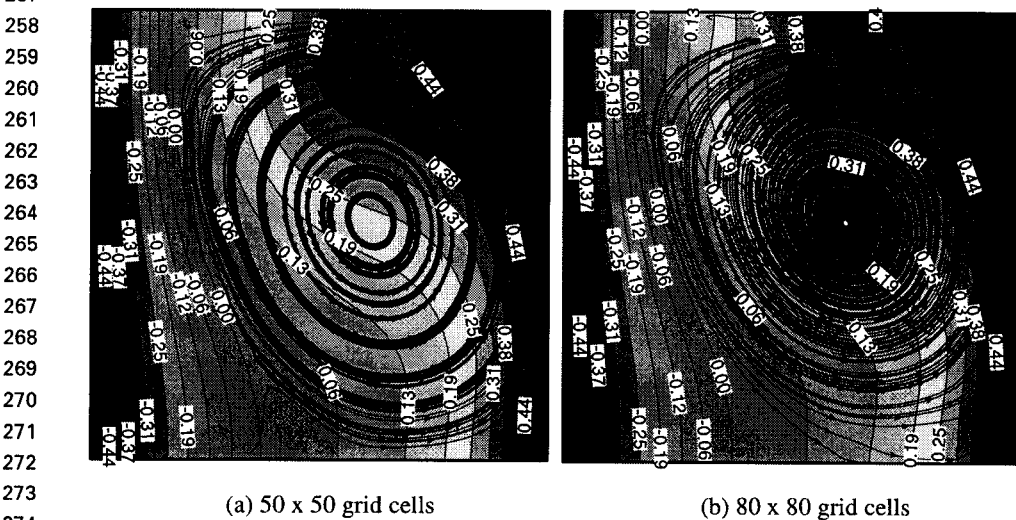
200031887_LMMP19_04_R1_081204

6   **S. Dulikravich et al.**

(a) 50 x 50 grid cells   (b) 80 x 80 grid cells

Figure 1. Temperature field and streamlines for smaller container using two grid sizes (Ht = 0.0).


(a) 50 x 50 grid cells   (b) 80 x 80 grid cells

Figure 2. Temperature field and streamlines for larger container using two grid sizes (Ht = 0.0).

OPTIMIZATION OBJECTIVES AND ALGORITHMS

A variety of optimization algorithms have been developed and used for problems from many different disciplines. Various optimization algorithms have

(a) Smaller container   (b) Larger container
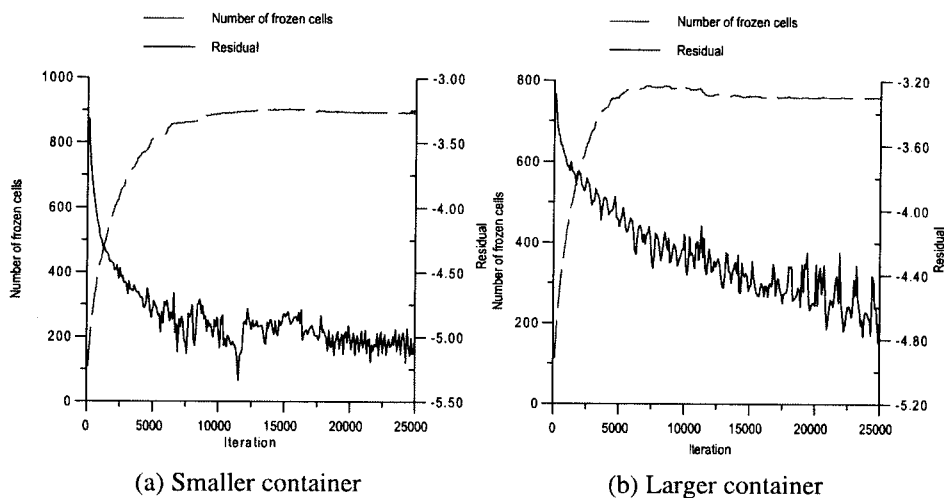
Figure 3. Convergence history for solidification in both containers (Ht = 0; grid 50 × 50 cells).

been known to provide different rates of convergence depending on the size and shape of the mathematical design space, the nature of the constraints, and where they are during the optimization process. This is why we created a hybrid constrained optimization computer program[10] that incorporates several of the most popular optimization modules: the Davidon-Fletcher-Powell (DFP) gradient search method, a genetic algorithm (GA), the Nelder-Mead (NM) simplex method, quasi-Newton algorithm of Pshenichny-Danilin (LM), differential evolution (DE), and sequential quadratic programming (SQP). The original package did not have the DE, SQP, and LM methods. A set of analytic rules were coded into the program to automatically switch among the different optimization algorithms to avoid local minima and to accelerate the overall convergence. Different versions of this hybrid optimization package have been successfully applied during the optimization of various multidisciplinary problems.[11] Another conceptually different optimizer, known as IOSO, was also used in this work. It is based on semi-stochastic methods and self-adaptive response surface methodology.[11,12] Different numerical analysis methods (finite volume and finite element methods) and different optimization algorithms (a hybrid optimizer and a IOSO optimizer) were used to demonstrate and compare their respective accuracies, robustness, and versatility.

MINIMIZATION OF THE NATURAL CONVECTION USING MHD AND A HYBRID OPTIMIZER

It is well known that application of a magnetic field to a solidifying flow-field of an electrically conducting fluid will create additional body forces that are

+   [12.8.2004–7:54pm]   [1–24]   [Page No. 8]
K./Journals/Inpro/MDI/LMMP/LMMP19(4)/200031887.3d   Materials and Manufacturing Processes (LMMP)

200031887_LMMP19_04_R1_081204

8   **S. Dulikravich et al.**

capable of significantly altering the flow-field and heat transfer.[13–16] It has also been demonstrated that it is possible to optimize the boundary values of the magnetic field with the objective of achieving certain desired features of the flow-field.[17,18] Let us now try to optimize the magnetic field applied on each of the four walls of the square container of test case 1 (smaller container) described in the previous section. The objective is to minimize the effects of the thermally induced natural convection in case of solidification from a sidewall. To satisfy magnetic flux conservation (Eq. 12), we consider the simple case of periodic boundary conditions.

$$B_1(0, y) = B_2(1, y) \tag{17}$$

$$B_3(x, 0) = B_4(x, 1) \tag{18}$$

The unknown boundary values of the magnetic field were parameterized as follows:

$$B(x_k) = \sum_{i=1}^{M} P_i C_i(x_k) \tag{19}$$

where P_i is unknown parameter and the function $C_i(x_k)$ is given as   **AQ3**

$$C_i(x_k) = \cos\left[(i-1)\frac{\pi}{2}x_k\right] \quad \text{for } i = 1, 3, 5, \ldots \tag{20}$$

$$C_i(x_k) = \cos\left[i\frac{\pi}{2}x_k\right] \quad \text{for } i = 2, 4, 6, \ldots \tag{21}$$

The objective function for this optimization problem was to minimize the sum of all vertical temperature gradient magnitudes in the entire liquid region that should minimize thermally induced buoyancy flow-field in the melt. Thus, our problem is to minimize the objective function, F, defined as

$$F = \left[\frac{1}{\#\text{liquid cells}} \sum_{i=1}^{\#\text{liquid cells}} \left(\frac{\partial T}{\partial y}\right)^2\right]^{1/2} \tag{22}$$

In all test cases, the initial guess for the parameters was zero, while the number of optimization population members was equal to three times the number of parameters. The hybrid optimizer started with the DE method in all test cases and the initial population was randomly generated around the initial guess.
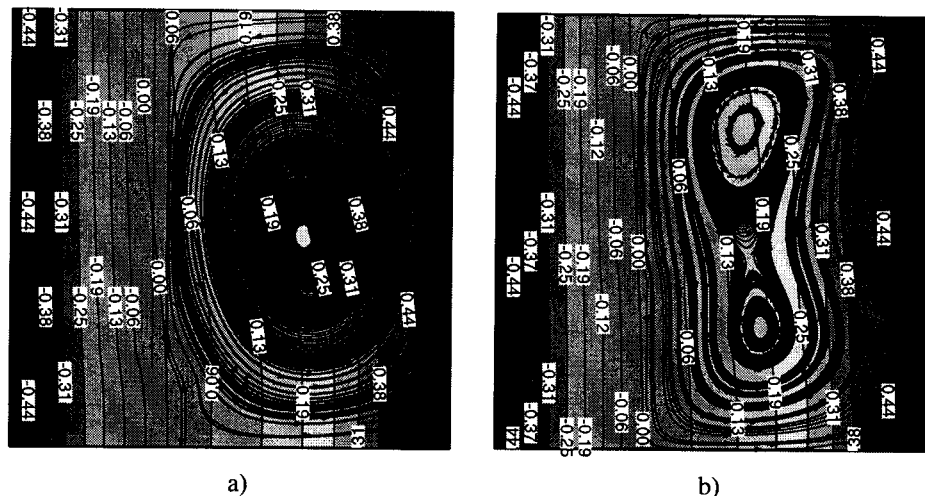
Figures 4a and b show the results for the test case 1 without an applied magnetic   **F4** field and with an optimized magnetic field applied. One can see that the buoyancy effects are reduced. In this test case, three parameters were used for $B_1(0, y)$ and three parameters were used for $B_3(x, 0)$. Figure 5 shows the optimized boundary   **F5** conditions, where one can see that the magnetic field is constant at the boundaries $y = 0.0$ and $y = 1.0$.
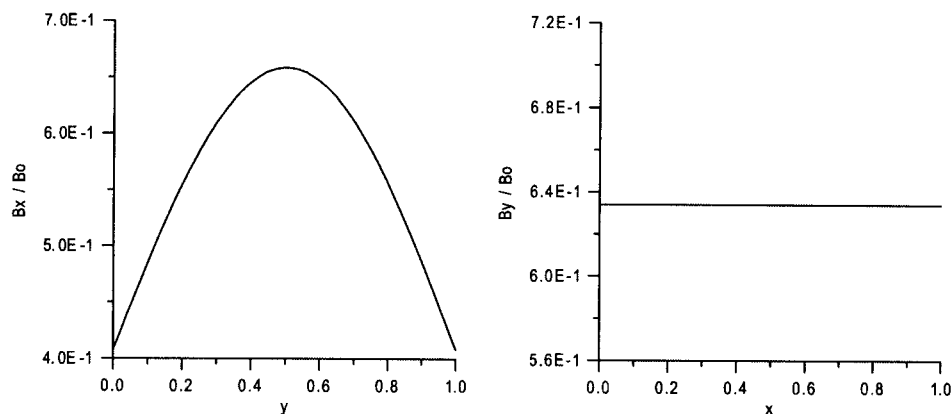
+ [12.8.2004—7:54pm]   [1–24]   [Page No. 9]
K:/Journals/Inpro/MDI/LMMP/LMMP19(4)/200031887.3d   Materials and Manufacturing Processes (LMMP)

200031887_LMMP19_04_R1_081204

Optimization of Intensities and Orientations   9

a)   b)

Figure 4. Isotherms and streamlines without: (a) and with (b) an optimized applied magnetic field (test case 1: smaller container).

Figure 5. Optimized magnetic field boundary conditions (test case 1: smaller container).
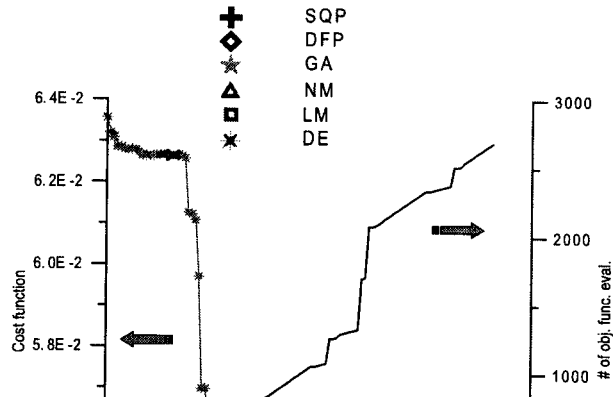
Figure 6 shows the convergence history for the hybrid optimizer in this case **F6** where the DE and NM optimization modules were automatically used most often.
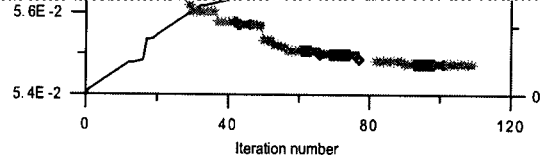
Figure 7 shows the results for test case 2 (a larger container) without an applied **F7** magnetic field and with an optimized magnetic field applied. One can see that the buoyancy effects are reduced, but not eliminated. Again, three parameters were used for $B_1(0, y)$ and three parameters for $B_3(x, 0)$, while periodic boundary conditions were enforced on the opposite boundaries. Figure 8 shows the optimized boundary **F8** conditions, where, again, the variation of the magnetic field along the boundaries $x = 0.0$ and $x = 1.0$ is greater than at the boundaries $y = 0.0$ and $y = 1.0$.
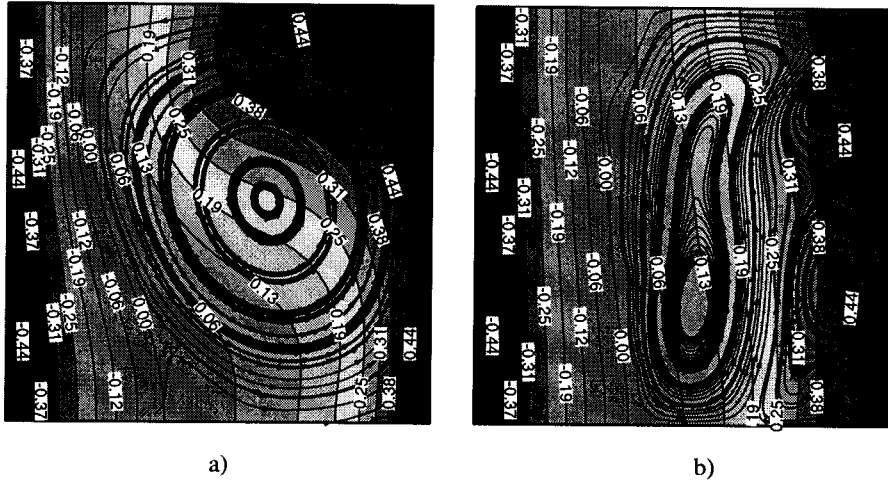
200031887_LMMP19_04_R1_081204

10

S. Dulikravich et al.

424
425
426
427
428
429
430
431
432
433
434
435
436

$+$ SQP
$\Diamond$ DFP
$\ast$ GA
$\triangle$ NM
$\square$ LM
$\ast$ DE

6.4E -2 — 3000

6.2E -2

6.0E -2 — 2000

5.8E -2

— 1000

Cost function

# of obj. func. eval.

Figure 6. Convergence history for the hybrid optimizer (test case 1: smaller container).

a)   b)

Figure 7. Isotherms and streamlines without: (a) and with (b) an optimized applied magnetic field (test case 2: larger container).

Figure 9 shows the convergence history for the hybrid optimizer in this test case where only the DE, GA, and NM optimization modules were automatically applied. **F9**
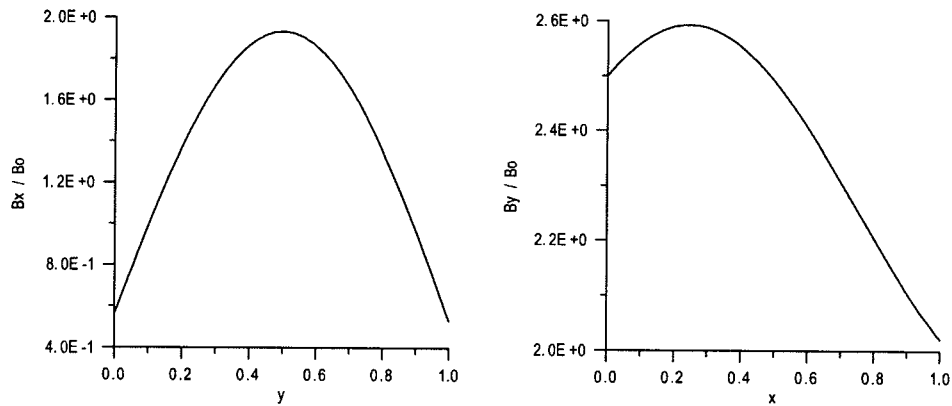
Figures 10 through 12 show the results for test case 2, but using six parameters for $B_1(0, y)$ and six parameters for $B_3(x, 0)$, instead of the three parameters used **F10–F12**
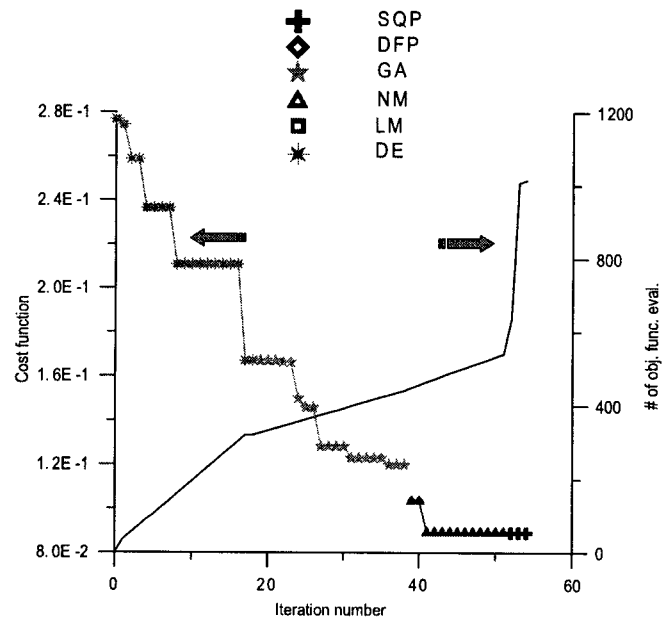
Optimization of Intensities and Orientations

471
472
473
474
475
476
477
478
479
480
481
482
483
484
485
486
487
488
489
490
491
492
493
494
495
496
497
498
499
500
501
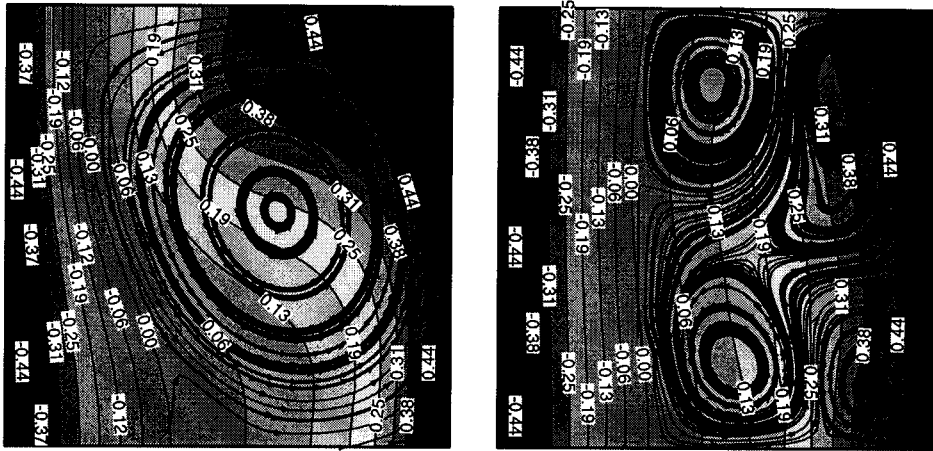502
503
504
505
506
507
508
509
510
511
512

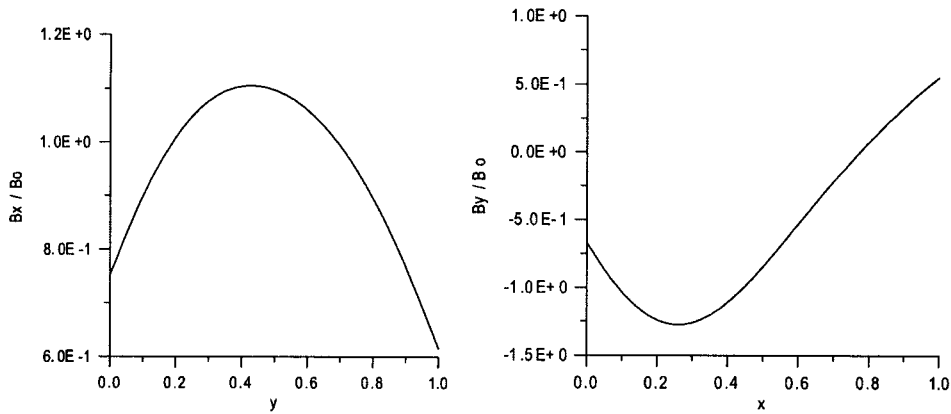**Figure 8.** Optimized magnetic field boundary conditions (test case 2: larger container).

Figure 9. Convergence history for the hybrid optimizer (test case 2: larger container).

513 before. One can see that the natural convection effects are further reduced in this
514 case. It is interesting to note that the variation of the applied magnetic field is greater
515 at the boundaries $y = 0.0$ and $y = 1.0$.
516   Figure 12 shows the convergence history, where, again, we applied the DE and
517 GA modules. In fact, the GA module did the entire job in this test case.

[12.8.2004–7:54pm]   [1–24]   [Page No. 12]
K./Journals/Inpro/MDI/LMMP/LMMP19(4)/200031887.3d   Materials and Manufacturing Processes (LMMP)

200031887_LMMP19_04_R1_081204

12   S. Dulikravich et al.

Figure 10. Isotherms and streamlines without and with an optimized applied magnetic field (test case 2 with six parameters).

Figure 11. Optimized magnetic field boundary conditions (test case 2 with six parameters).

MHD SOLIDIFICATION OPTIMIZATION USING LSFEM AND IOSO OPTIMIZER

Other possibly more robust and accurate numerical integration methods were explored[14,15] to allow for physical values of the magnetic Prandtl number and for significantly higher values of viscosity in the solid region. Consequently, we will present a combination of MHD with solidification where the numerical analysis was performed with a least squares spectral finite element method (LSFEM),[15,18] and

565
566
567
568
569
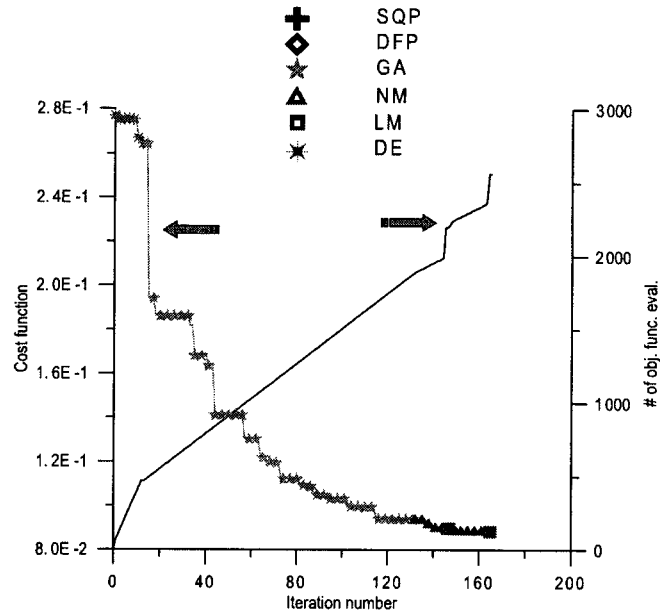570
571
572
573
574
575
576
577
578
579
580
581
582
583
584
585
586

Figure 12. Convergence history for the hybrid optimizer (test case 2 with six sensors).

587
588
589   the optimization was performed using a self-adaptive response surface-based semi-   **AQ4**
590   stochastic algorithm[11,12] called IOSO. Here, the objective of the optimization is to
591   minimize the velocity magnitude of the melt flow near the solid-liquid interface. The
592   optimizer searches for this by changing the orientation and distribution of the
593   sidewall magnets as well as the strength of the applied external uniform vertical
594   magnetic field. The objective function was expressed as the following equation:
595
596
597     $$F = \sum_{i=1}^{N_{\text{fluid}}} \sqrt{u_i^2 + v_i^2} \qquad\qquad (23)$$
598
599   Here, N_{fluid} is the total number of grid points located between $y > 0.04$ m and
600     $y < 0.08$ m—that is, only in the flow-field region adjacent to the solid/melt interface.
601   The only constraints considered in this problem were the bounds on the magnitudes
602   of the design variables. In this problem, we considered a container with relatively
603   weak magnets embedded in the sidewalls. The magnetic flux density strength and
604   distribution was parameterized using a B-spline with control variables located at
605   7 points along the wall ($y = 0.0$, 0.02, 0.04, 0.06, 0.08, 0.1 m). These design variables
606   controlled the magnitude, direction, and distribution of the magnetic field.
607   Two cases were run. For case 1, each control point was allowed to vary from
608   0.07 Tesla to −0.07 Tesla. In case 2, each control point was allowed to vary from 0.5
609   Tesla to −0.5 Tesla. This distribution was applied to the right wall. The distribution
610   on the left wall was taken to be of equal magnitude, but opposite sign to that of the
611   right wall. Therefore, the resulting magnetic field was always symmetrical with

14   **S. Dulikravich et al.**

612 respect to the *y*-axis. A vertical magnetic field was also applied so that it could be
613 generated using an electromagnet located on the top and bottom of the container.
614 The optimized magnetic potential produced a uniform vertical field strength varying
615 between 0.0 Tesla to 0.15 Tesla in case 1 and between 0.0 Tesla and 0.5 Tesla in
616 case 2. For this example, the total number of design variables was seven.
617   The optimization procedure was applied to the solidification of a silicon melt in a
618 square container with sides of 0.1 m. A uniform temperature of 1676.0 K was applied
619 to the top wall so that solidification occurred on the top wall of the container.
620 A parabolic temperature profile was applied to the hot bottom of the container
621 to simulate nonuniform heating of the melt. The temperature at the center of the
622 bottom wall was 1688.0 K, and the temperature at the bottom corners was set to
623 1686.0 K. The sidewalls were thermally insulated. A no-slip condition for velocity
624 was enforced on all walls of the container. The magnetic flux density determined
625 from the B-spline parameterization was specified directly on the sidewalls.
626 A constant magnetic potential was specified on the top and bottom of the container.
627 The potentials were determined by calculating the potential required to produce a
628 uniform vertical field of a specified strength. A relatively coarse quadrilateral
629 computational grid with $17 \times 17 = 289$ elements with a p-level of $P = 3$ was used with
630 the LSFEM code (Fig. 13).   **F13**
631
632   The p-version of LSFEM was used to compute all results reported here. The
633 order of the approximation function was increased, or enriched, until the desired
634 level of convergence was obtained. In this case, the size of the grid was fixed and the
635 order of the approximation was increased uniformly across the grid. For problems
636 with smooth solutions, the p-version of the LSFEM converged to the exact solution
637 at an exponential rate as the number of unknowns was increased by the uniform
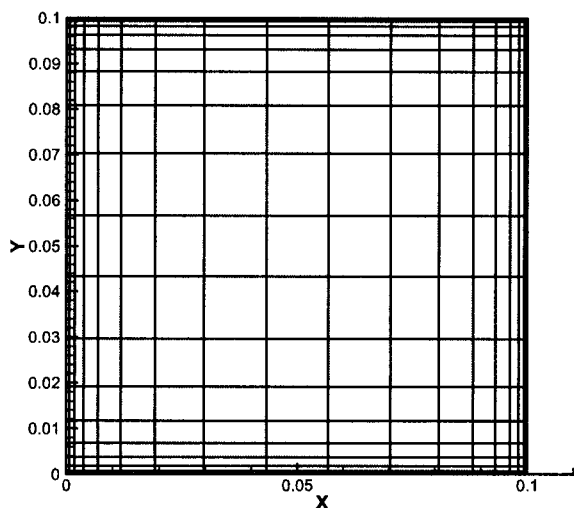638 enrichment of the element approximation functions.
639
640
641
642
643
644
645
646
647
648
649
650
651
652
653
654
655
656
657
658

Figure 13. Computational grid for FEM analysis.

Optimization of Intensities and Orientations

<div align="right">15</div>

In cases where the mushy region was only one grid cell wide, the effective heat capacity including the latent heat release was computed using an enthalpy method.[15,19]

$$\rho C^{eq} = \frac{dH}{dT} \approx \frac{|\nabla H|}{|\nabla T|} \tag{24}$$

Using this treatment in the mush region allowed much larger values of the viscosity to be specified in the solid phase. Specifically, LSFEM/MHD solidification with the enthalpy method used seven orders of magnitude higher viscosity in the solid phase than in the liquid phase. Figures 14 and 15 show velocity field and streamlines
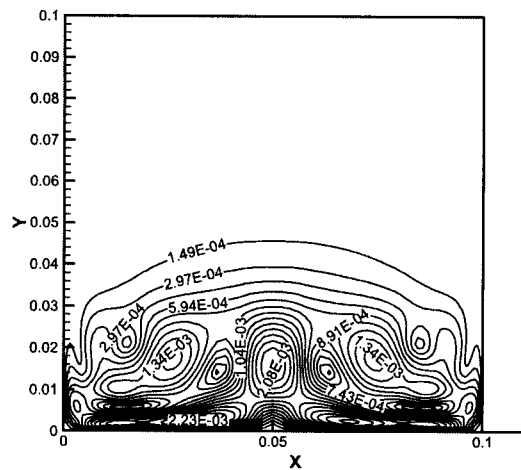
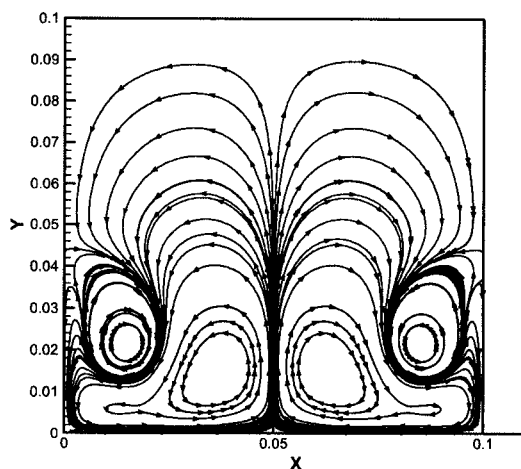***Figure 14.*** Velocity magnitudes with no applied magnetic field—FEM analysis.

Figure 15. Streamlines with no applied magnetic field—FEM analysis.

[12.8.2004–7:54pm]

K./Journals/Inpro/MDI/LMMP/LMMP19(4)/200031887.3d

[1–24]

Materials and Manufacturing Processes (LMMP)

[Page No. 16]

200031887_LMMP19_04_R1_081204

706 computed without the application of a magnetic field. Correct physical value of
707 the magnetic Prandtl number was used in all simulations based on LSFEM/MHD.
708   The IOSO algorithm was used to optimize the applied magnetic field to this
709 problem.[12,11] The optimization code was executed on a commodity component-
710 based parallel computer with Pentium II processors (400 MHz speed). Twenty   **AQ5**
711 processors were used, and the total execution time was about 16 h. The initial guess
712 given to the optimizer was that all design variables were set to zero. In other words,
713 the initial guess was a flow-field without any applied magnetic field. In that case the
714 normalized value of the objective function is 1.0.

715
716
717
718   **LSFEM: Case 1**
719
720   In this case, the sidewall magnetic field strengths were very weak. They varied
721 between 0.07 T and 0.07 T. A maximum strength for uniform vertical field varied
722 between 0.0 T and 0.15 T. After 12 iterations, the IOSO-based optimizer achieved its
723 best objective function value of 0.292. In comparison, the objective function for a
724 simple case of no sidewall magnets and a maximum strength uniform vertical field of
725 0.15 T achieved a value of 0.771. The optimized magnetic field reduced the average
726 velocity in the melt region between $y = 0.04$ m and $y = 0.08$ m by more than a factor
727 of three. Figures 16 and 17 demonstrate that the magnetic field effectively damped   **F16 F17**
728 the flow field circulation, removing the pair of secondary vortices present in the case
729 with no applied magnetic field. Figure 18 shows the optimized magnetic field lines   **F18**
730 of flux density.
731   In the lower half of the sidewall, the magnets were at maximum strength of
732 0.07 T. Above that, the polarity changed and the strength of the sidewall magnet was
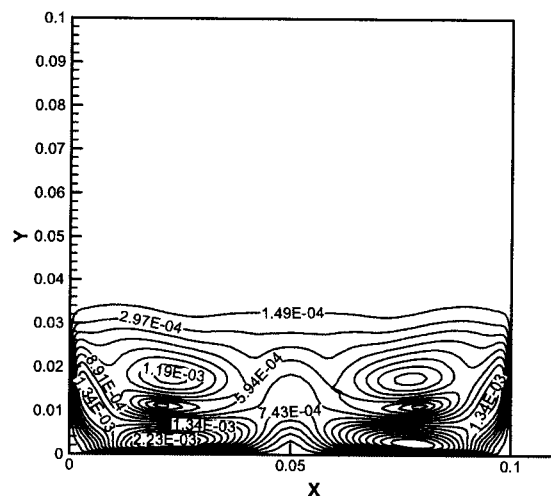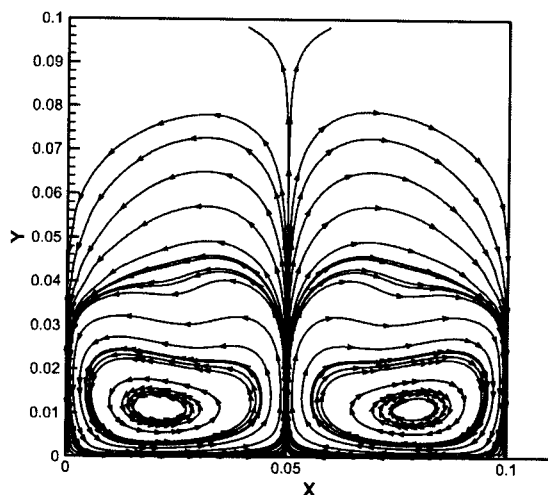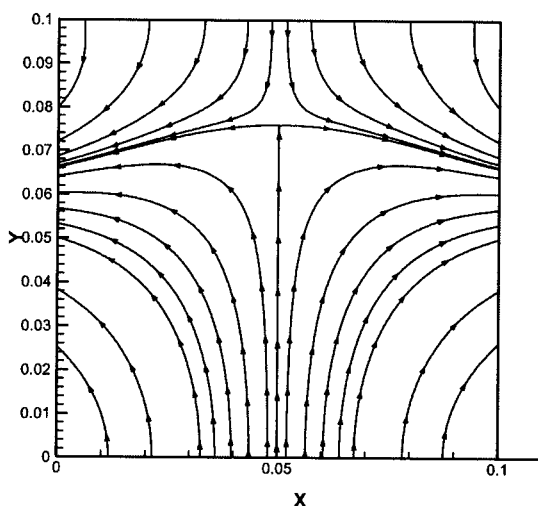733 reduced to 0.04 T at the top of the container (Fig. 19). For the top and bottom walls,   **F19**
734
735
736
737
738
739
740
741
742
743
744
745
746
747
748
749
750
751
752

Figure 16. Velocity magnitudes with optimized applied magnetic field (case 1).

[12.8.2004—7:54pm]   [1—24]   [Page No. 17]
K:/Journals/Inpro/MDI/LMMP/LMMP19(4)/200031887.3d   Materials and Manufacturing Processes (LMMP)

200031887_LMMP19_04_R1_081204

Optimization of Intensities and Orientations   17

753
754
755
756
757
758
759
760
761
762
763
764
765
766
767
768
769
770

Figure 17. Streamlines with optimized applied magnetic field (case 1).

771
772
773
774
775
776
777
778
779
780
781
782
783
784
785
786
787
788
789
790

Figure 18. Lines of magnetic flux for the optimized applied magnetic field (case 1).
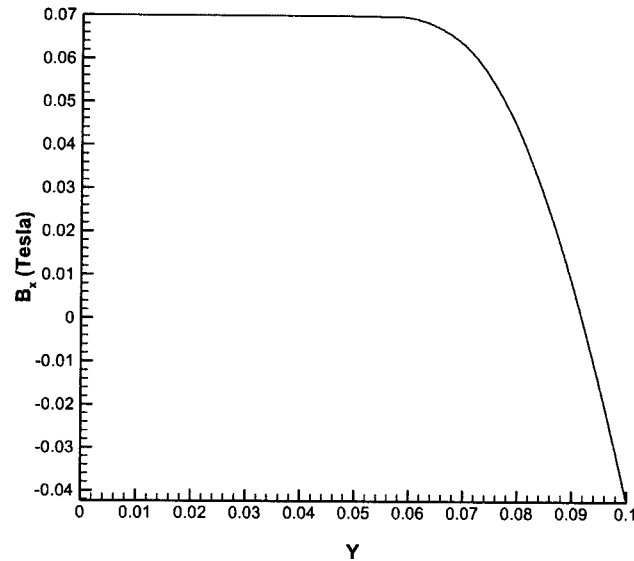
791
792

793   the optimizer chose a magnetic potential that would produce a uniform vertical field
794   of 0.025 T. This is interesting since the optimizer had the choice of producing up to
795   0.15 T but yet converged to a much smaller value. This indicates that by damping the
796   melt circulation, the shape of the magnetic field was as important as its strong
797   vertical component. Figure 20 compares the temperature distribution between flow   **F20**
798   with no magnetic field and flow with optimized magnetic field. The optimized field
799   clearly smoothes the temperature contours due to the reduced convection.
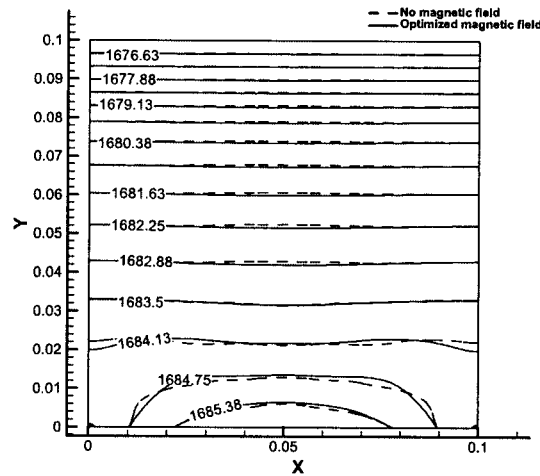
+ [12.8.2004–7:54pm] [1–24] [Page No. 18]
K./Journals/Inpro/MDI/LMMP/LMMP19(4)/200031887.3d Materials and Manufacturing Processes (LMMP)

200031887_LMMP19_04_R1_081204

18 **S. Dulikravich et al.**

Figure 19. Distribution of B_x along the right wall for the optimized applied magnetic field (case 1).
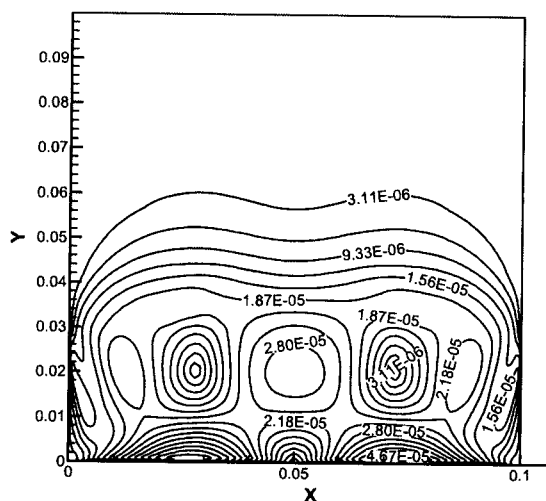

Figure 20. Comparison of isotherms with optimized applied magnetic field and with no applied magnetic field (case 1).
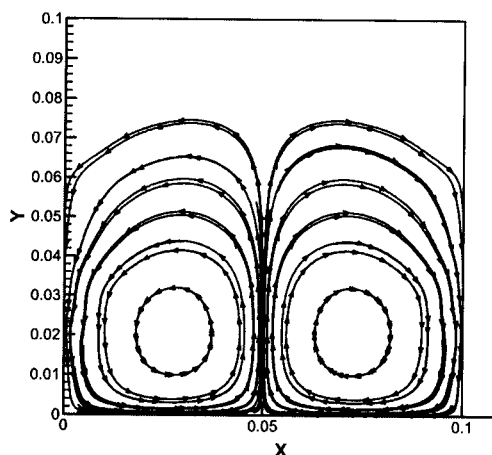
LSFEM: Case 2

In case 2, the sidewall magnetic field strengths varied between $-0.5\,\text{T}$ and $0.5\,\text{T}$, while the maximum strength for the uniform vertical field was allowed to vary

847
848
849
850
851
852
853
854
855
856
857
858
859
860
861
862
863
864
865

Figure 21. Velocity magnitudes with optimized applied magnetic field (case 2).

866
867
868
869
870
871
872
873
874
875
876
877
878
879
880
881

Figure 22. Streamlines with optimized applied magnetic field (case 2).

882
883
884

885 between 0.0 T and 0.5 T. Thus, case 2 differed from case 1 by allowing for wider
886 ranges of boundary values for the applied magnetic field. After 14 iterations, the
887 IOSO-based optimizer achieved a best objective function of value 0.111. In this case,
888 the optimized magnetic field reduced the average velocity in the melt region between
889 $y = 0.04$ m and $y = 0.08$ m by more than a factor of 9 (Figs. 21 and 22). Figure 23
890 shows the magnetic field lines of flux density that correspond to the optimized
891 magnetic field boundary conditions (Fig. 24). All of the wall magnets were at maxi-
892 mum strength of 0.5 T. On the top and bottom walls, the optimizer converged to
893 a magnetic potential that would produce a uniform vertical field of 0.5 T. These
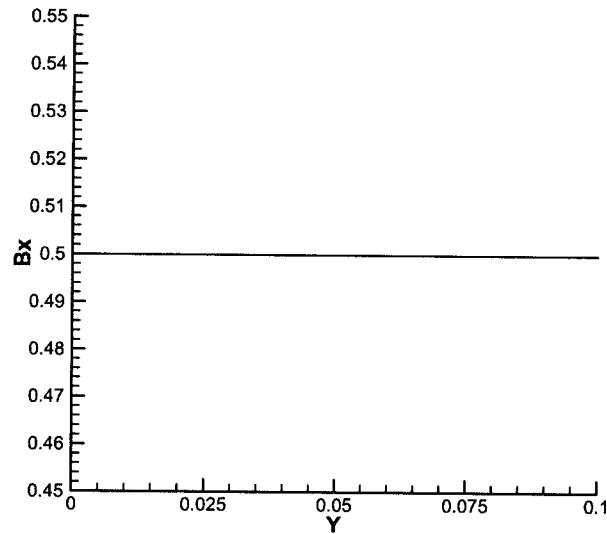
F21–F23
F24

200031887_LMMP19_04_R1_081204

20

S. Dulikravich et al.

894
895
896
897
898
899
900
901
902
903
904
905
906
907
908
909
910
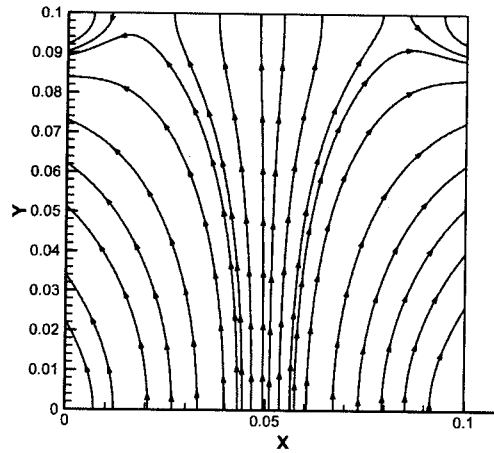
Figure 23. Lines of magnetic flux for the optimized applied magnetic field (case 2).

911
912
913
914
915
916
917
918
919
920
921
922
923
924
925
926
927
928
929
930
931

Figure 24. Distribution of B_x along the right wall for the optimized applied magnetic field (case 2).

932
933
934
935
936
937
938
939
940

optimized magnetic field boundary conditions have effectively damped out the flow field circulation, removing the pair of secondary vortices that were present with no applied magnetic field. Figure 25 compares the temperature distribution in the solid and liquid phases. The optimized field clearly changes the temperature contours due to the reduced convection and the suppression of the secondary vortices. The optimized thermal field was very close to the temperature distribution that would be obtained by pure heat conduction.

F25

[12.8.2004–7:54pm]   [1–24]   [Page No. 21]
K:/Journals/Inpro/MDI/LMMP/LMMP19(4)/200031887.3d   Materials and Manufacturing Processes (LMMP)

200031887_LMMP19_04_R1_081204

941
942
943
944
945
946
947
948
949
950
951
952
953
954
955
956
957
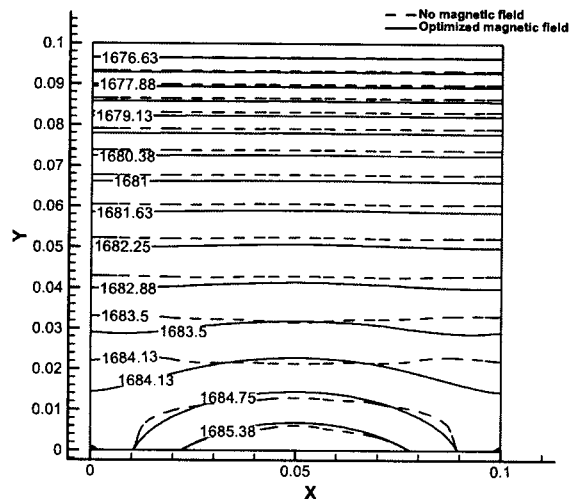
958 **Figure 25.** Comparison of isotherms with optimized applied magnetic field and with no
959 applied magnetic field (case 2).

960
961

SUMMARY

964   The feasibility of a new concept for controlling solidification processes during
965 manufacturing of defect-free crystals by the optimization of the distributions and
966 orientations of magnets along the boundaries of a solidification container has been
967 demonstrated. The simultaneous analysis of the magneto-hydro-dynamics of the
968 melt flow-field and the accrued solid was performed using two very different
969 numerical algorithms: a finite volume algorithm, and a least-squares finite element
970 algorithm. LSFEM method was able to reduce the average melt circulation velocity
971 by a factor of 9, effectively generating a thermal field very close to a distribution that
972 would be produced by pure heat conduction. This method was also more robust
973 because it allowed for physical values of the magnetic Prandtl number and for
974 extremely high value of viscosity in the solid region. Two methods for treating
975 the mushy region were also exercised: an equivalent specific heat formulation and
976 an enthalpy method. The enthalpy method appears to be more robust. The param-
977 eterized boundary values of the magnetic field were optimized by two entirely
978 different optimization algorithms: a hybrid constrained optimization algorithm and
979 a novel self-adaptive response surface semi-stochastic optimization algorithm.
980 The IOSO optimizer required substantially smaller number of MHD solidification
981 analysis. This minimization was achieved by optimizing a finite number of param-
982 eters describing analytically the distribution and the orientations of the boundary
983 values of the magnetic field. For cases where solidification begins at the top wall and
984 at a sidewall, the methodology was shown to reduce the intensity of the melt velocity
985 by creating new shapes of the melt/solid interface in prespecified parts of the flow-
986 field. Formulations of other objective functions and multi-objective optimization
987 involving simultaneous optimization of magnetic and thermal boundary conditions

[12.8.2004–7:54pm]   [1–24]   [Page No. 22]
K./Journals/Inpro/MDI/LMMP/LMMP19(4)/200031887.3d   Materials and Manufacturing Processes (LMMP)

200031887_LMMP19_04_R1_081204

22   S. Dulikravich et al.

should be possible. Future work should focus on experimental verification of these numerical results since this concept could be extended to controlled manufacturing of three-dimensional functionally graded material objects.

ACKNOWLEDGEMENTS

NOMENCLATURE

$\underline{B}$	Magnetic flux density, $\mathrm{kg\,A^{-1}\,s^{-2}}$
c	Specific heat at constant pressure, $\mathrm{J\,kg^{-1}\,K^{-1}}$
$\underline{g}$	Acceleration due to gravity, $\mathrm{m\,s^{-2}}$
H	Enthalpy per unit volume, $\mathrm{J\,m^{-3}}$
$\underline{H} = \underline{B}/\mu_o - \underline{M}$	Magnetic field intensity, $\mathrm{A\,m^{-1}}$
$\underline{J}$	Electric current density, $\mathrm{A\,m^{-2}}$
L	Latent heat of phase change per unit mass, $\mathrm{m^2\,s^{-2}}$
$\underline{M}$	Total magnetization per unit volume, $\mathrm{A\,m^{-1}}$
p	Pressure, $\mathrm{kg\,m^{-1}\,s^{-2}}$
T	Absolute temperature, K
$\underline{v}$	Fluid velocity, $\mathrm{m\,s^{-1}}$

Greek Symbols

α	Volumetric thermal expansion coefficient, $\mathrm{K^{-1}}$
κ	Thermal conductivity coefficient, $\mathrm{kg\,m\,s^{-3}\,K^{-1}}$
σ	Electric conductivity coefficient, $\mathrm{kg^{-1}\,m^{-3}\,s^3\,A^2}$
ρ	Fluid density, $\mathrm{kg\,m^{-3}}$
μ	Magnetic permeability coefficient, $\mathrm{kg\,m\,A^{-2}\,s^{-2}}$
μ_v	Shear coefficient of viscosity, $\mathrm{kg\,m^{-1}\,s^{-1}}$
$\tilde{\theta}$	Non-dimensional temperature (Eq. 1)
θ	Non-dimensional temperature (Eq. 2)

Subscripts

s	Solid phase
l	Liquid phase
mix	Liquid–solid mixture (mushy zone)
r	Reference value
liquidus	Corresponding to liquidus temperature
solidus	Corresponding to solidus temperature
h	Hot surface of the container
c	Cold surface of the container

[12.8.2004–7:54pm] [1–24] [Page No. 23]
K:/Journals/Inpro/MDI/LMMP/LMMP19(4)/200031887.3d Materials and Manufacturing Processes (LMMP)

200031887_LMMP19_04_R1_081204

Optimization of Intensities and Orientations 23

REFERENCES

1. Sampath, R.; Zabaras, N. Inverse thermal design of thermo-magnetically driven boussinesq flows. ASME National Heat Transfer Conference, Pittsburgh, PA, August 20–22, 2000.

2. Voller, V.R.; Swaminathan, C.R. General source-based method for solidification phase change. Numerical Heat Transfer Part B **1991**, *19*, 175–189.

3. Poirier, D.; Salcudean, M. On numerical methods used in mathematical modeling of phase change in liquid metals. ASME paper 86-WAM/HT-22, Anaheim, CA, December 7–12, 1986.

4. Gray, D.D.; Giorgini, A. The validity of the Boussinesq approximation for liquids and gases. International Journal of Heat and Mass Transfer **1976**, *19*, 545–551.

5. Dulikravich, G.S.; Lynn, S.R. Unified electro-magneto-fluid dynamics (EMFD): a survey of mathematical models. International Journal of Non-Linear Mechanics **1995**, *32* (5), 923–932.

6. Dulikravich, G.S. Electro-magneto-hydrodynamics and solidification, Chapter 9, In *Advances in Flow and Rheology of Non-Newtonian Fluids*, Part B; Siginer, D.A., De Kee, D., Chhabra, R.P., Eds.; Rheology Series, 8, Elsevier, June, 1999; 677–716.   AQ6

7. Ko, H.-J.; Dulikravich, G.S. A fully non-linear model of electro-magneto-hydrodynamics. International Journal of Non-Linear Mechanics **2000**, *35* (4), 709–719.

8. Bird, R.B.; Stewart, W.E.; Lightfoot, E.N. *Transport phenomena*; John Wiley and Sons, Inc.: New York, London, 1960.   AQ7

9. Dulikravich, G.S.; Ahuja, V.; Lee, S. Modeling three-dimensional solidification with magnetic fields and reduced gravity. International Journal of Heat and Mass Transfer **1994**, *37* (5), 837–853.

10. Dulikravich, G.S.; Martin, T.J.; Dennis, B.H.; Foster, N.F. Multidisciplinary hybrid constrained GA optimization, Chapter 12, In *EUROGEN'99—Evolutionary Algorithms in Engineering and Computer Science: Recent Advances and Industrial Applications*; Miettinen, K., Makela, M.M., Neittaanmaki, P., Periaux, J., Eds.; John Wiley and Sons, Jyvaskyla, Finland, May 30–June 3, 1999; 233–259.

11. Dulikravich, G.S.; Dennis, B.H.; Martin, T.J.; Egorov, I.N. Multi-disciplinary design optimization. In *Invited Lecture at EUROGEN 2001—Evolutionary Methods for Design, Optimization and Control with Applications to Industrial Problems*; Giannakoglou, K., Tsahalis, D.T., Periaux, J., Fogarty, T., Eds.; Published by International Center for Numerical Methods in Engineering (CIMNE), Barcelona, Spain: Athens, Greece, Sept, 19–21, 2002; 11–18.

12. Egorov, I.N. Indirect optimization method on the basis of self-organization. Proceedings of International Conference on, Optimization Techniques and Applications (ICOTA'98), Curtin University of Technology, Perth, Australia, 1998, 683–691.

13. Motakeff, S. Magnetic field elimination of convective interference with segregation during vertical-bridgman growth of doped semiconductors. Journal of Crystal Growth **1990**, *104*, 833–850.

24   S. Dulikravich et al.

1082   14.   Fedoseyev, K.I.; Kansa, E.J.; Marin, C.; Ostrogorsky, A.G. Magnetic field
1083   suppression of semiconductor melt flow in crystal growth: Comparison of three
1084   methods for numerical modeling. Japanese CFD Journal **2001**, *9*, 325–333.
1085   15.   Dennis, B.H.; Dulikravich, G.S. Magnetic field suppression of melt flow in
1086   crystal growth. International Journal of Heat and Fluid Flow **2002**, *23* (3),
1087   269–277.
1088   16.   Dennis, B.H.; Dulikravich, G.S. Simulation of magnetohydrodynamics with
1089   conjugate heat transfer. Proceedings of ECCOMAS2000—European Congress
1090   on Computational Methods in Applied Sciences and Engineering, Barcelona,
1091   Spain, September, 11–14; Onate, E., Bugeda, G., Suarez, B., Eds.; 2000.
1092   17.   Dulikravich, G.S.; Choi, K.-Y.; Lee, S. Magnetic field control of vorticity in
1093   steady incompressible laminar flows. Symposium on Developments in Elec-
1094   trorheological Flows and Measurement Uncertainty, IL, Chicago, November
1095   6–11, 1994; Siginer, D.A., Kim, J.H., Sheriff, S.A., Colleman, H.W., Eds.;
1096   ASME FED-Vol. 205/AMD-Vol. 190, ASME WAM'94, 125–142.
1097   18.   Dennis, B.H.; Dulikravich, G.S. Optimization of magneto-hydrodynamic
1098   control of diffuser flows using micro-genetic algorithm and least squares
1099   finite elements. Journal of Finite Elements in Analysis and Design **2001**, *37* (5),
1100   349–363.
1101   19.   Morgan, K.; Lewis, R.W.; Zienkiewicz, O.C. An improved algorithm for
1102   heat conduction and problems with phase change. International Journal for
1103   Numerical Methods in Engineering **1977**, 1191–1195.
1104
1105
1106
1107
1108
1109
1110
1111
1112
1113
1114
1115
1116
1117
1118
1119
1120
1121
1122
1123
1124
1125
1126
1127
1128